USB Proceedings

2014 International Conference on Electrical Machines (ICEM)

Andel`s Hotel Berlin
Berlin, Germany
02 - 05 September, 2014

Sponsored by

The Institute of Electrical and Electronics Engineers (IEEE)
IEEE Industrial Electronics Society (IES)

Co-sponsored by

ETG - Power Engineering Society withing VDI

Contactless power supply for magnetically levitated elevator systems using a SMC hybrid actuator

R. Appunn and Kay Hameyer

***Abstract*—A contactless power supply (CPS) for the cabin of a magnetically levitated elevator is presented in this paper. In contrast to commercial stand-alone contactless power supply systems, a combined CPS and electromagnetic guiding system (MGS) is introduced. The inductive energy transmission is realized by utilizing the magnetic circuit of an actuator of the linear guiding. With this approach two devices are combined into one unit. The hybrid actuator consists of an omega shaped yoke, fabricated of soft magnetic composites (SMC), with permanent magnets and coils on its lateral arms. A concentrated primary winding is added to the guide rail and a coil wound around the central arm of the omega actuator functions as secondary winding. Hereby a superposition of the MGS flux and the CPS flux emerges in the magnetic circuit of the actuator and the transmission path is established. The proposed system requires less construction space and weight when compared to existing energy transmission systems.**

***Index Terms*—Contactless power supply, control, hybrid actuator, inductive energy transmission, linear guiding, magnetic levitation (maglev), soft magnetic composites (SMC)**

NOMENCLATURE

δ_x	Air gap displacement in x-direction
δ_y	Air gap displacement in y-direction
η	Efficiency of the CPS
$\mathbf{L}$	Inductance matrix
μ_r	Relative permeability
ω_0	Resonant frequency of the CPS
Ψ_p	Flux linkage of the primary coil
Ψ_s	Flux linkage of the secondary coil
$\underline{Z}_r$	Reflected impedance
C_p	Primary capacitance
C_s	Secondary capacitance
k	Coupling coefficient
L_p	Primary self inductance
L_s	Secondary self inductance
M	Mutual inductance
N_p	Number of primary windings
N_s	Number of secondary windings
P_{core}	SMC and PM losses
P_{in}	Input power
P_{loss}	Total losses
P_{out}	Output power
Q_p	Primary quality factor
Q_s	Secondary quality factor
R_L	Load resistance
R_p	Primary coil resistance

978-1-4799-4775-1/14/$31.00 ©2014 IEEE

Institute of Electrical Machines (IEM), RWTH Aachen University, Schinkelstr. 4, D-52056 Aachen, Germany

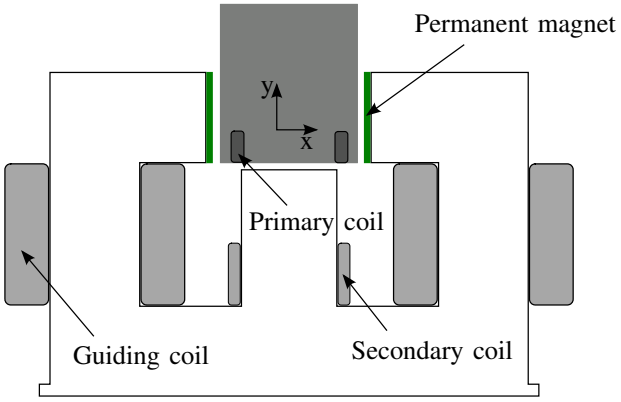

Fig. 1. Schematic layout of the Ω-actuator with separate secondary coil.

I. INTRODUCTION

Contactless power transmission enhances the benefits of electromagnetically levitated systems such as wearless operation by eliminating sliding contacts or traveling cables [1], [2]. Electromagnetically levitated trains or other fast moving vehicles are able to consume power via harmonics induced by the propulsion device mounted to the guide way [3]. For slow vehicles this concept does not suite, here an extra induction rail in the guide way and additional coils on the vehicle have to be constructed. In automotive systems one can find similar approaches [4], [5]. Recent studies for automatic guided vehicle systems even use quadrature pick-up systems [6]. Hereby the horizontal and vertical component of the magnetic field can be utilized for the power transfer. Other recent research investigates bidirectional inductively coupled power transfer systems for electric vehicle applications and focuses on the synchronization of primary and secondary converters [7], [8]. For contactless battery charging Zhong et. al. propose a planar CPS system with high tolerances due to the position of the battery [9]. All autonomous CPS systems yields extra cost and requires additional construction space.

At the Institute of Electrical Machines (IEM) a ropeless elevator test bench with a linear drive and electromagnetic guiding is built. The linear drive is realized by two long stator permanent magnet synchronous motors diagonally placed on the elevator shaft [10]. An air gap winding is applied to eliminate strong normal forces. On the moving part, the cabin, only permanent magnets need to be attached. The guiding system consists of four Ω-actuators with two

(DOF) control [12] for the translational and rotatory DOF of the elevator car. The design and control of the MGS are described in detail in [13].

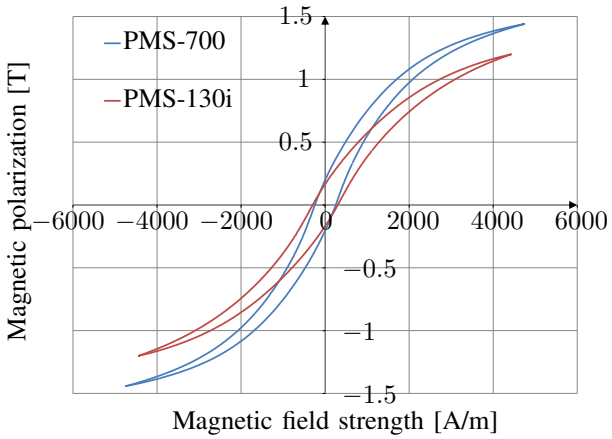

Fig. 2. Hysteresis curves of the materials PMS-700 and PMS-130i (manufacturer names).

A power transmission is designed to supply the cabin of the ropeless elevator. A nominal load of $200W$ has to be transferred to supply the MGS coils and the on-board electronic components in the cabin such as eddy current sensors and current controllers.

In previous studies an integrated solution of guiding and power transmission to minimize both, cost and space is considered [14]. The authors investigated a similar strategy in [15]. On the central arm of one of the guiding actuators, an additional coil is placed. This coil functions as secondary winding for the energy transmission system. A concentrated coil is integrated into the guide rail of the system. It produces a high frequency EM field, which superposes the levitating field. Hereby, a voltage is induced in the secondary coils mounted to the moving part and the power supply of the vehicle is established. Thereby, an integrated solution for both, contactless guiding and contactless power transmission using existing components is found. Figure 1 shows the topology.

A major drawback of this combined guiding and power transmission actuator has been identified. The core losses in the laminated steel of the actuator are critically high. To overcome this drawback the use of soft magnetic composites (SMC) is proposed and studied by the authors. SMC is commonly used in axial flux machines [16], [17] or tubular actuators [18] where laminated steel cannot be utilized, since the magnetic flux path is 3-dimensional. This material has a slightly lower saturation when compared to laminated steel but significantly lower eddy current losses, which is an advantage regarding the high supply frequency. This means an actuator consisting of this SMC material would be bigger when compared to the one made from laminated steel. The larger dimensions of the actuator result in a lower amplitude of the magnetic flux density created by the primary coil of the inductive power supply. This is an additional advantage since the losses in the SMC core will be further reduced.

II. Soft Magnetic Composites

SMC consists of small metal swarf in the range of several μm. These swarf are immersed in insulation and adhesive. Due to this fabrication, very few eddy currents can arise, the efficiency of electrical machines can be increased. There are several drawbacks using SMC. The relative permeability is less compared to iron. Due to the fabrication process,

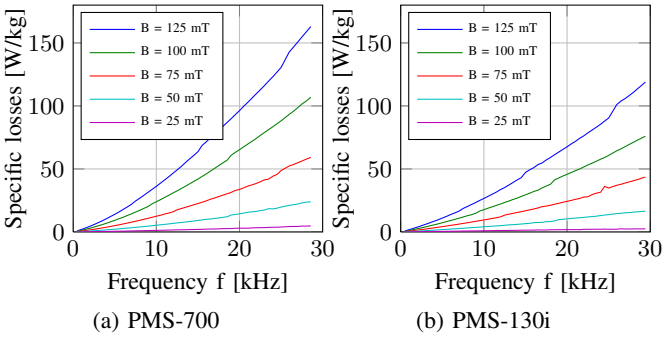

Fig. 3. Losses of the SMC material.

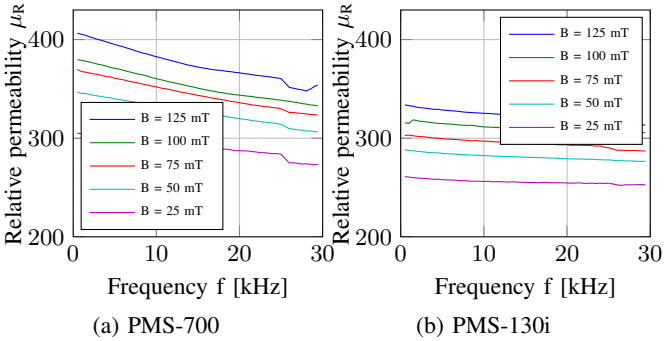

Fig. 4. Relative permeability of the SMC material.

SMC is brittle [20]. The breaking strength is approximately $100Mpa$ which is smaller than iron (approximately $300MPa$). SMC is pressed into standard shapes, which are converted afterwards, Hereby grinding, milling and drilling is used. Due to the topology of the omega shaped actuator with the integrated power supply, a compromise regarding the material characteristics must be found. On the one hand a high saturation polarization is required, on the other hand the losses must be low. To determine an appropriate SMC, two material samples are characterized on a core tester at the institute. One sample is optimized for high polarization (PMG-700), the other one is optimized regarding low losses (PMG-130i).

A. Characterization of soft magnetic composites

The hysteresis loops of the two ring samples are measured at the test bench at a frequency of $50Hz$ The saturation of both materials can be seen in figure 2. PMG-700 has a maximum flux density of $1.4T$ at $4000^A/_m$. The flux density of PMG-130i at the same magnetic field strength is only $1.2T$.

To determine the material losses, the loss characteristics regarding frequency and flux density are measured. At fixed amplitudes of the flux density, the frequency is swept from $500Hz$ to $29kHz$. Figure 3(a) depicts the measurement values of PMS-700. The losses rise quadratically with the frequency but linearly with the amplitude. Up to $5kHz$ the specific losses of PMS-700 are below $20^W/_{kg}$ and thereby very low. Regarding higher frequency, the losses rise significantly to $165^W/_{kg}$ at $29kHz$ and $125mT$. At $25mT$ the losses are even at $29kHz$ comparatively small, the overall losses are smaller. At $29kHz$ and $125mT$ the losses are $120^W/_{kg}$. $40^W/_{kg}$ smaller compared to PMS-700. Figure 3(b) shows the measurement results of PMS-130i.

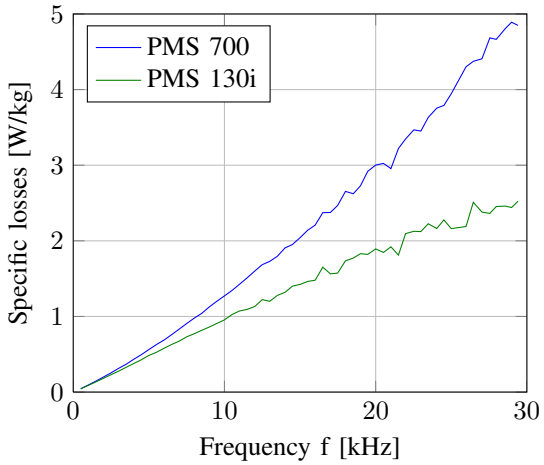

Fig. 5. Comparison of the specific losses at 25 mT.

The relative permeability of the two SMC probes is measured at the material test bench as well. Figure 4(a) depicts the relative permeability of PMS-700 regarding different values of frequency and flux density. There is only a slight dependency of the frequency. PMS-700 has a relative permeability of 400 at $500Hz$. At $29kHz$ μ_r is fallen about 10% to 350. The relative permeability depends more on the amplitude of the flux density than the material losses. At $125mT$ μ_r is 410, at $25mT$ the value is fallen to 305, both at a frequency of $500Hz$. Here, the characteristics of PMS-130i are similar, as well (compare figure 4(b)). The relative permeability at $500Hz$ and $125mT$ is 330. Compared to PMS-700, the frequency dependency is smaller. The decrease of μ_r from $500Hz$ to $29kHz$ is only 3%.

After the characterization of the materials, the most appropriate one for the application i.e. the actuator has to be determined. On the one hand a high relative permeability and saturation polarization is required for the linear guiding operation. On the other hand higher losses are disadvantageous for the energy transmission. For the application of the energy transmission only small amplitudes of the flux density are utilized, since the cross section of the actuator is large, due to the required guiding forces. The losses at a small flux density of $B = 25mT$ are studied in detail. Figure 5 depicts the specific losses of PMS-700 and PMS-130i at $25mT$. In the lower frequency region the material losses are close to each other. At $12kHz$ the rise of the losses of PMS-700 is higher when compared to PMS-130i. At $29kHz$ the specific losses of PMS-700 are $4.75^{W}/_{kg}$, the material PMS-130i has only losses of $4^{W}/_{kg}$. This difference is very small and negligible for the case of application studied.

From the measurements it can be concluded:

- For the aspect of the linear guiding PMS-700 is preferred due to its higher saturation polarization
- Regarding the energy transmission capability, the losses at the working point are smaller using PMS-130i. But the differences between the materials is negligible

Due to the aforementioned considerations, the actuator is fabricated from PMS-700 and the transmission frequency ω_0 is set to $25kHz$.

The CPS is modeled using a Π-equivalent circuit with self and mutual inductances, winding resistances and a parallel resistance describing the core losses. The following differential equation system characterizes the transmission path:

$$\begin{pmatrix} u_p \\ u_s \end{pmatrix} = \begin{pmatrix} R_p & 0 \\ 0 & R_s \end{pmatrix} \begin{pmatrix} i_p \\ i_s \end{pmatrix} + \partial_t \begin{pmatrix} \Psi_p \\ \Psi_s \end{pmatrix} \tag{1}$$

with the winding resistances $R_{p,s}$. The time-derivative of the flux linkages is given by:

$$\partial_t \begin{pmatrix} \Psi_p \\ \Psi_s \end{pmatrix} = \partial_{\mathbf{i}} \begin{pmatrix} \Psi_p \\ \Psi_s \end{pmatrix} \cdot \partial_t \begin{pmatrix} i_p \\ i_s \end{pmatrix}. \tag{2}$$

Regarding the operation of the considered CPS system the SMC material is not saturated. Therefore the derivative $\partial_{\mathbf{i}} \boldsymbol{\Psi}$ is constant, this yields:

$$\partial_{\mathbf{i}} \begin{pmatrix} \Psi_p \\ \Psi_s \end{pmatrix} = \mathbf{L} = \begin{pmatrix} L_p & -M \\ -M & L_s \end{pmatrix}. \tag{3}$$

$\mathbf{L}$ is the inductance matrix including primary and secondary self inductances and the mutual inductances. The magnetic coupling can be characterized by the coupling coefficient,

$$k = \frac{M}{\sqrt{L_s \cdot L_p}}. \tag{4}$$

In contrast to the model of transformers, and due to the relative large air gap, the coupling coefficient of contactless power supply systems is much smaller.

The inductance matrices of various design variations are determined using finite element calculations. Herewith a high accuracy is achieved and the study of the power transmission capability of the system can be performed. The inductances are extracted as described in [21]. Because of the linear B-H characteristic in the range of operation the tangent inductance matrix is equal to the secant one [21]. To consider the different axial length of the long guide rail and the short omega actuator it is not sufficient to generate a 2D FE model. Hence a 3D FE model of the actuator is constructed. Once the inductance matrix is extracted for the linear case all points of operation can be calculated analytically in the same accuracy as performed by a computational FE computation. A coupling of the FE model to a circuit simulator of the power electronics is not required.

IV. Topology of the Transmission Path

The existing topology of the Ω-actuator is enhanced by both primary and secondary winding. The primary winding is integrated into a SMC-block within the guide rail (compare figure 12). The secondary winding is placed around the central yoke of the actuator. There are various possibilities to position both coils. Each one can either be placed outside i.e. around the block/yoke or buried within a slot. Four topologies are presented: *poso* (primary outside, secondary outside), *posi*,*piso* and *pisi*. The four topologies are depicted in figure 6.

In addition to the position of the coils, the number of windings can be varied, too. Since the frequency of the power transmission is very high and the space for the coils is limited, configurations with high number of turns are not feasible. The following winding configurations are considered: *p05s05* (number of primary windings $N_p = 5$, *p07s07*, *p07s15*, *p10s05*, *p10s10*, *p12s12*, *p15s05*, *p15s07* and *p15s15*. For the presented configurations the inductance matrix is extracted by finite element calculation. Hereby the

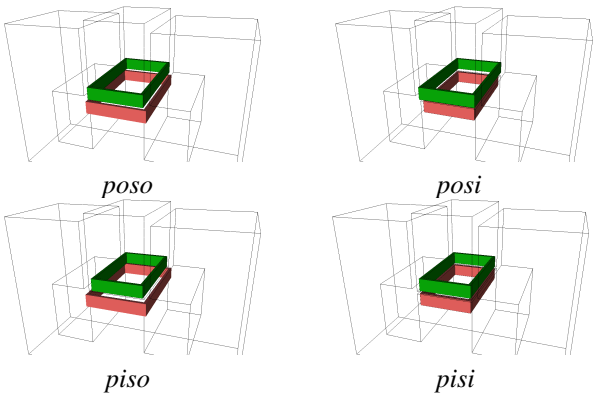

Fig. 6. Comparison of the topologies (green: primary coil, red: secondary coil).

coupling factor and the maximum transmittable power is calculated. From the simulation several conclusions can be drawn:

Coupling factor The coupling factor is a geometry depending parameter, it is determined by the flux path i.e. the magnetic circuit. The *poso* topology has the highest coupling factor. The pole area of both coils is larger when compared to the other topologies and the magnetic circuit is not interrupted by slots.

Self inductance The self inductances are independent from each other, since the coil inductance depends quadratically on the number of turns and the magnetic circuit. The core material (SMC) and the air gaps influence the magnetic circuit. The differences between the topologies vary only slightly. The inductances of the topologies with buried secondary coil is smaller, since the effective air gap is increased.

Leakage Depending on the topology the coils do not face each other exactly. With buried secondary windings the pole area decreases and the flux created by the primary coil flows not through the secondary coil exclusively. There are flux components which close through the air, i.e. leakage flux components. The coupling decreases because of these flux components. Figure 7 depicts the effect of leakage flux.

Buried coils The possibility of integrating the coils into slots within the guide rail or the central yoke of the actuator reduces the amount of required space and leads to a more robust placement of the coils. Regarding the whole system the disadvantage of the buried topology becomes apparent. The self inductances increase and the mutual inductance decreases, leading to a smaller coupling coefficient. The magnetic flux is short-circuited through the web at the upper coil edge. Figure 8 shows this effect. In figure 8 (left) both

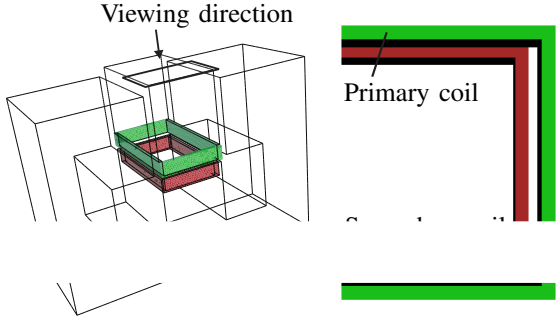

Fig. 7. Different coil cross sections using *posi* topology.

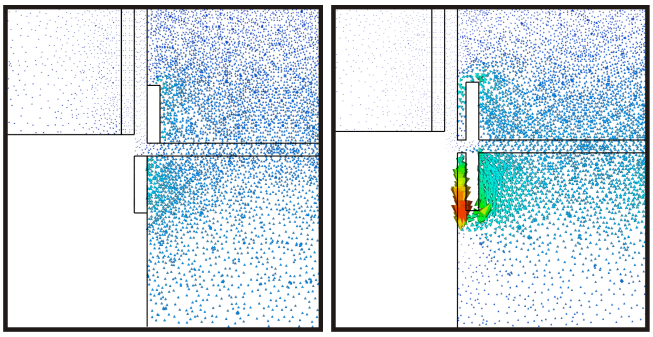

Fig. 8. Flux paths of the different topologies.

coils are placed outside and the secondary coil is powered. The major part of the magnetic flux flows through the primary and secondary coil. The coupling coefficient is quite high ($k = 0.83$). In figure 8 (right) the flux density in the web is high (short-circuit path) and the part of the flux which flows through the primary coil is smaller compared to the *poso* topology.

To fulfill the power requirements only three possible topologies can be identified. The configurations *p15s07, p15s05* and *p10s05* of the *poso* topology offer a sufficient power transmission capability. Considering the stability of the system, only the configuration *p15s05* fulfills the requirements, compare section VI-C.

V. Deviations from working point

The design and simulation of the transmission path is done for the nominal position of the cabin in its equilibrium in the center of the shaft. In this case all air gap lengths are $3mm$. In case of external forces applied to the cabin, a temporary displacement of the air gaps occurs. This leads to a disturbance of the magnetic circuit and therewith to a variation of the inductance matrix. Concerning the stability of the system, the sensitivity of the inductance matrix regarding position deviations, is critical. In various simulations the position of the actuator is varied in steps of $0.25mm$ up to a maximum displacement of $1mm$ in both spatial directions. Figures 9,10 and 11 depict the resulting primary (L_p), secondary (L_s) and mutual inductance (M), respectively.

From simulation the following conclusions can be drawn. The air gap deviation in y-direction has a stronger influence on the inductances than the deviation in x-direction. With increasing air gap in y-direction the inductances decrease. At maximum deviation of $1mm$ all three inductances vary approximately by 15%. In x-direction the resulting air gap is constant, due to the ω-actuator geometry. One of the two air gaps in x-direction increases the other one decreases. Different leakage paths lead to a slight variation of the inductance matrix of $< 1\%$ in x-direction. The considered system is robust. In nominal operation the deviation of the inductance matrix is negligible and even strong displacements result in a maximum deviation of 10% of the resonance frequency.

To verify the design process, the power transmission capability of the SMC actuator is measured. Figure 12 shows the actuator including primary and secondary windings. First

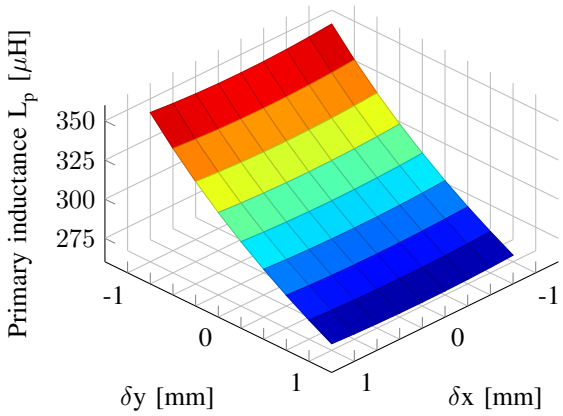

Fig. 9. Variation of primary inductance L_p.

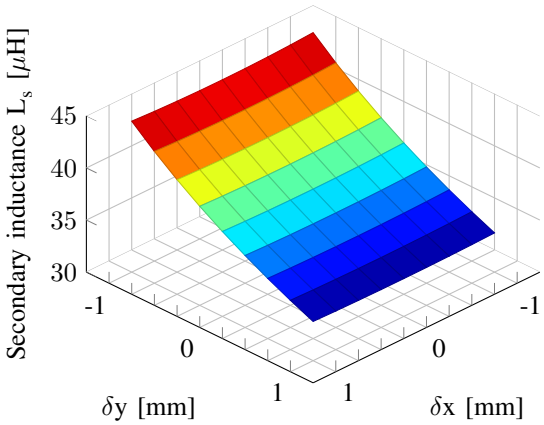

Fig. 10. Variation of secondary inductance L_s.

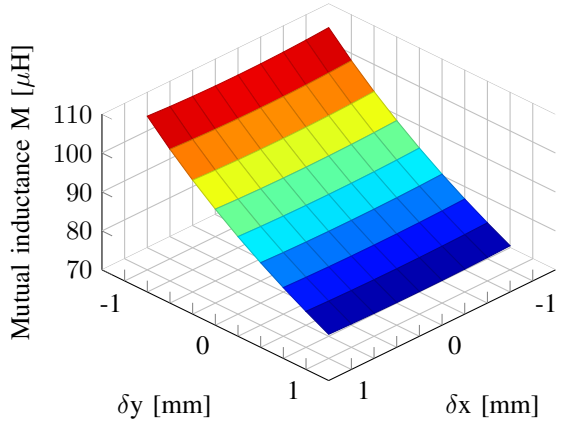

Fig. 11. Variation of mutual inductance M.

measurements without permanent magnets are performed to separate the core losses from eddy current losses of the permanent magnets. Thereafter the magnets are attached and the regular topology is measured, as well.

A. Measurement of the inductance matrix

From no-load measurements the parameter of the inductance matrix are determined [15]. Table I compares the simulated and measured quantities. The simulated values differ by 20% – 27%. This deviation results from the prototype structure of the actuator. On the one hand the actuator could not be constructed exactly according to the simulation model. It is built from single SMC cuboids connected with adhesive, which means additional air gaps. On the other hand the coils are wound by hand and do not match the exact geometric dimensions. This explains the deviation of simulation and measurement. When comparing the simulation with the measurements with permanent magnets, the inductances decrease further. Due to the eddy currents induced into the magnets at the operation frequency of $25kHz$ which are not considered in simulation, the flux created by the primary winding is reduced and additional losses occur.

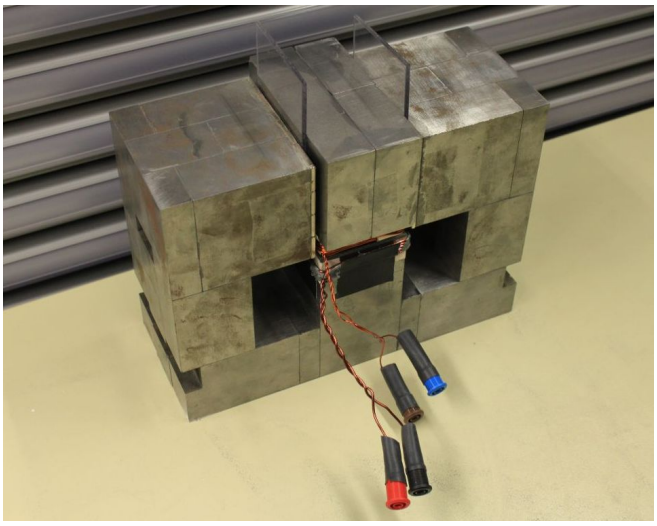

Fig. 12. Omega actuator constructed of SMC cuboids.

TABLE I
COMPARISON OF SIMULATED AND MEASURED INDUCTANCES.

Inductance	sim.	meas. without PM	dev.	meas. with PM	dev.
$L_p[\mu H]$	299	240	20 %	199	33 %
$L_s[\mu H]$	37	30	19 %	28	24 %
$M[\mu H]$	89	65	27 %	55	38 %

B. Loss determination

The core losses of the SMC and the aforementioned eddy current losses in the permanent magnets are determined from no-load measurements. The loss separation is possible since measurements with and without permanent magnets are performed. From the phase shift between voltage and current on the primary side the core losses can be determined. Without permanent magnets core losses of $12,26W$ occur, when applying a voltage of $67V$ on the primary side. Including the permanent magnets, additional $12,74W$ losses occur. From various operation points it can be seen, that the losses split into equal parts between the two materials. In addition ohmic losses arise in primary and secondary coils, according to the winding resistances of $R_p = 112m\Omega$ and $R_s = 48m\Omega$, respectively.

C. Reactive power compensation

required to eliminate the reactive input power demand and to transfer only active power over the air gap. Capacitances are connected to primary and secondary windings. Various

topologies are discussed in literature [22]. The secondary compensation capacitance is always given by

$$C_s = \frac{1}{\omega^2 L_s}. \tag{5}$$

Using a serial compensation, the impedance of the secondary is neutralized and the secondary voltage becomes load independent. Herewith the compensated secondary resembles a voltage source. This compensation topology is often used when feeding a DC-link [23]. Using a parallel compensation, the admittance of the secondary is neutralized and the secondary current becomes load independent. The secondary resembles a current source which can be used for battery charging [24]. The positioning of the secondary compensation capacitance affects the reflective impedance $\underline{Z}_r$ and therewith the quality factors. Equation 6 describes the reflected impedance $\underline{Z}_r$ for both positioning:

$$\underline{Z}_r = \begin{cases} \frac{(\omega M)^2}{R_L} & \text{Serial} \\ \left(\frac{M}{L_s}\right)^2 R_L - j\omega\frac{M^2}{L_s} & \text{Parallel} \end{cases} \tag{6}$$

The quality factor depicts the ratio of the reactive power in primary or secondary circuit and the delivered active power. There is a primary Q_p and secondary quality factor Q_s. They can be determined by the following equations:

$$Q_p = \frac{i_p^2 \omega L_p}{i_p^2 \Re\{\underline{Z}_r\}} \quad \text{and} \quad Q_s = \frac{i_s^2 \omega L_s}{i_p^2 \Re\{\underline{Z}_r\}}. \tag{7}$$

For system stability $Q_p >> Q_s$ is required [25]. The primary compensation is depending on the secondary one. If the secondary circuit has a serial compensation $\Im\{\underline{Z}_r\} = 0$. This leads to a primary compensation capacitance

$$C_p = \begin{cases} \frac{1}{\omega^2 L_p} & \text{Serial} \\ \frac{L_p}{\omega^2\left(\left(\frac{M^2}{R_L}\right)^2 + L_P^2\right)} & \text{Parallel} \end{cases} \tag{8}$$

For a parallel compensation of the secondary circuit $\Im\{\underline{Z}_r\} = -j\omega\frac{M^2}{L_s}$. Now the primary compensation capacitance follows

$$C_p = \begin{cases} \frac{1}{\omega^2\left(L_p - \frac{M^2}{L_s}\right)} & \text{Serial} \\ \frac{L_p - \frac{M^2}{L_s}}{\left(\left(\frac{M}{L_s}\right)^2 R_L\right)^2 + \omega^2\left(L_p - \frac{M^2}{L_s}\right)^2} & \text{Parallel} \end{cases} \tag{9}$$

After the determination of the core loss resistance, the compensation topologies can be compared by simulation (Table II).

TABLE II
SIMULATIVE COMPARISON OF THE COMPENSATION TOPOLOGIES.

Topology	P_{in}	P_{out}	P_{loss}	P_{core}	η
serial-serial	230,7	148,7	71,75	68,9	64,5 %
serial-parallel	205,5	167,7	33,75	30,7	81,6 %
parallel-serial	664,5	427	203	197,5	64,25 %
parallel-parallel	341,7	281,2	55,86	51,77	82,3 %

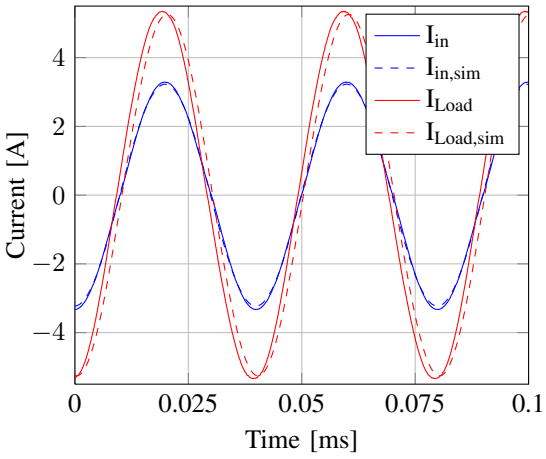

Fig. 13. Currents of the transmission path.

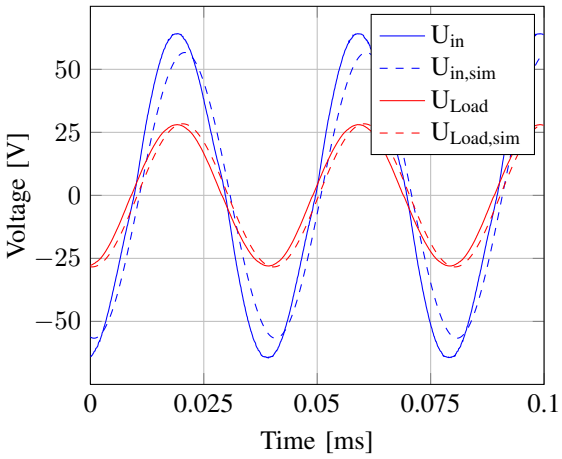

Fig. 14. Voltages of the transmission path.

gies have a low efficiency of 64%. The topologies with parallel compensation on the secondary side have a considerably higher efficiency of 82%. Depending on the compensation topology, the reflected impedance $\underline{Z}_r$ changes, resulting in a higher voltage drop over the core loss resistance. This means higher core losses and the efficiency decreases. The input power of the primary serial compensated topologies is far lower when compared to the topologies with primary parallel compensation. The reason is the input impedance, which depends on the compensation topology. Simulated losses are depicted and the dominant loss factor, the core losses are shown. They consists of material losses in the SMC and the eddy current losses of the permanent magnets.

D. Energy transmission

The CPS is built using SP-topology parameterized from the measured inductances and sinusoidal currents are applied. A load resistance $R_L = 5,4\Omega$ reflects the inner resistance of 50 lithium-polymer battery-cells connected in series (including a dc-converter) which can provide $185V$ to power the guiding actuators and onboard electronics. Figures 13 and 14 show the simulated and measured electrical quantities on input and load of the transmission path, respectively. A good correlation between simulation and measurement is shown. The voltage requirement is 7% higher than simulated.

actly. With a transmittable power of $75W$ an efficiency of 73% is reached. Regarding a combined actuator for guiding and simultaneously for energy transmission, this value is acceptable.

VII. Conclusions

This paper gives a detailed analysis in the redesign of a combined magnetic guiding system and contactless power supply actuator entity for a vertical transportation vehicle, such as an elevator system. The use of SMC for the core material is introduced. Material probes are measured and the most appropriate one is selected. Various design variations are analyzed by means of the finite element method. A prototype is built and the contactless energy transmission is demonstrated. Compared to former designs the core losses could be significantly reduced. Simulation and measurement show good correlation. This topology augments the benefits of a ropeless elevator with a linear drive and contactless guiding by eliminating any physical contact to the shaft. In future works the actuator will replace a guiding actuator of the elevator test bench at the institute and the energy transfer will be tested within operation of the magnetic guiding system.

References

[1] J. Smeets, T. Overboom, J. Jansen, and E. Lomonova, "Modeling framework for contactless energy transfer systems for linear actuators," *Industrial Electronics, IEEE Transactions on*, vol. 60, no. 1, pp. 391 –399, jan. 2013.

[2] J. de Boeij, E. Lomonova, J. Duarte, and A. Vandenput, "Contactless energy transfer to a moving actuator," in *Industry Applications Conference, 2006. 41st IAS Annual Meeting. Conference Record of the 2006 IEEE*, vol. 4, oct. 2006, pp. 2020 –2025.

[3] J.-Y. Lee, I.-J. Lee, J.-W. Kim, J.-H. Chang, D.-H. Kang, S.-U. Chung, and J.-P. Hong, "Contactless power transfer system combined with linear electric machine," in *Electrical Machines and Systems, 2007. ICEMS. International Conference on*, 2007, pp. 1544 –1548.

[4] J. Sallan, J. L. Villa, A. Llombart, and J. F. Sanz, "Optimal design of icpt systems applied to electric vehicle battery charge," *IEEE Transactions on Industrial Electronics*, vol. 56, no. 6, pp. 2140–2149, June 2009.

[5] G. Covic, J. Boys, M. Kissin, and H. Lu, "A three-phase inductive power transfer system for roadway-powered vehicles," *IEEE Transactions on Industrial Electronics*, vol. 54, no. 6, pp. 3370–3378, Dec. 2007.

[6] S. Raabe and G. Covic, "Practical design considerations for contactless power transfer quadrature pick-ups," *Industrial Electronics, IEEE Transactions on*, vol. 60, no. 1, pp. 400 –409, jan. 2013.

[7] D. Thrimawithana, U. Madawala, and M. Neath, "A synchronization technique for bidirectional ipt systems," *Industrial Electronics, IEEE Transactions on*, vol. 60, no. 1, pp. 301 –309, jan. 2013.

[8] U. Madawala, M. Neath, and D. Thrimawithana, "A power-frequency controller for bidirectional inductive power transfer systems," *Industrial Electronics, IEEE Transactions on*, vol. 60, no. 1, pp. 310 –317, jan. 2013.

[9] W. Zhong, X. Liu, and S. Hui, "A novel single-layer winding array and receiver coil structure for contactless battery charging systems with free-positioning and localized charging features," *Industrial Electronics, IEEE Transactions on*, vol. 58, no. 9, pp. 4136 –4144, sept. 2011.

[10] M. Platen and G. Henneberger, "Examination of leakage and end effects in a linear synchronous motor for vertical transportation by means of finite element computation," *IEEE Transactions on Magnetics*, vol. 37, no. 5, pp. 3640–3643, September 2001.

[11] M. Morishita and M. Akashi, "Electromagnetic non-contact guide system for elevator cars," in *The Third International Symposium on*

[12] A. S. Ghersin and R. S. Sánchez Peña, "LPV Control of a 6-DOF Vehicle," *IEEE Transactions on Control Systems Technology*, vol. 10, no. 6, pp. 883–887, November 2002.

[13] R. Appunn, B. Schmülling, and K. Hameyer, "Electromagnetic Guiding of Vertical Transportation Vehicles: Experimental Evaluation," *IEEE Trans. on Industrial Electronics*, vol. 57, no. 1, pp. 335–343, January 2010.

[14] B. Schmülling and K. Hameyer, "PowerTRACE - a Novel Power Transmission and Actuator Entity," in *20th International Conference on Magnetically Levitated Systems and Linear Drives, MAGLEV*, San Diego, USA, December 2008, pp. 15–18.

[15] R. Appunn, B. Riemer, and K. Hameyer, "Contactless power supply for magnetically levitated elevator systems," in *Electrical Machines (ICEM), 2012 XXth International Conference on*, Sept 2012, pp. 600–605.

[16] R. Di Stefano and F. Marignetti, "Electromagnetic analysis of axial-flux permanent magnet synchronous machines with fractional windings with experimental validation," *Industrial Electronics, IEEE Transactions on*, vol. 59, no. 6, pp. 2573 –2582, june 2012.

[17] G. De Donato, F. Capponi, and F. Caricchi, "No-load performance of axial flux permanent magnet machines mounting magnetic wedges," *Industrial Electronics, IEEE Transactions on*, vol. 59, no. 10, pp. 3768 –3779, oct. 2012.

[18] F. Marignetti, S. Carbone, V. Delli Colli, and C. Attaianese, "Cryogenic characterization of copper-wound linear tubular actuators," *Industrial Electronics, IEEE Transactions on*, vol. 59, no. 5, pp. 2167 –2177, may 2012.

[19] T. A. Lipo, S. M. Madani, and R. White, "Soft magnetic composigtes for ac machines - a fresh perspective," University of Wisconsin, Wisconsin Electric Machines & Power Electronics Consortium, Tech. Rep. 2004-26, 2005.

[20] E. Fleischer and W. Hofmann, "Application of soft magnetic composites in active magnetic bearings," in *IECON 2011 - 37th Annual Conference on IEEE Industrial Electronics Society*, 2011, pp. 1770–1775.

[21] E. Lange, F. Henrotte, and K. Hameyer, "An efficient field-circuit coupling based on a temporary linearization of fe electrical machine models," *Magnetics, IEEE Transactions on*, vol. 45, no. 3, pp. 1258 –1261, 2009.

[22] C.-S. Wang, O. Stielau, and G. Covic, "Design considerations for a contactless electric vehicle battery charger," *Industrial Electronics, IEEE Transactions on*, vol. 52, no. 5, pp. 1308 – 1314, 2005.

[23] A. Kelley and W. Owens, "Connectorless power supply for an aircraft-passenger entertainment system," *Power Electronics, IEEE Transactions on*, vol. 4, no. 3, pp. 348–354, 1989.

[24] R. Laouamer, M. Brunello, J.-p. Ferrieux, O. Normand, and N. Buchheit, "A multi-resonant converter for non-contact charging with electromagnetic coupling," in *Industrial Electronics, Control and Instrumentation, 1997. IECON 97. 23rd International Conference on*, vol. 2, 1997, pp. 792–797 vol.2.

[25] O. Stielau and G. Covic, "Design of loosely coupled inductive power transfer systems," in *Power System Technology, 2000. Proceedings. PowerCon 2000. International Conference on*, vol. 1, 2000, pp. 85 –90 vol.1.

VIII. Biographies

Ruediger Appunn received the diploma in electrical engineering from the Faculty of Electrical Engineering and Information Technology, RWTH Aachen University, Aachen, Germany, in 2008. Since 2008, he has been a researcher, since 2010 group leader with the Institute of Electrical Machines, RWTH Aachen University. His research fields include magnetic levitation, mechatronics and control.

Kay Hameyer Dr. Kay Hameyer received his M.Sc. degree in electrical engineering from the University of Hannover and his Ph.D. degree from the Berlin University of Technology, Germany. After his university studies he worked with the Robert Bosch GmbH in Stuttgart, Germany as a Design Engineer for permanent magnet servo motors and vehicle board net components. Until 2004 Dr. Hameyer was a full Professor for Numerical Field Computations and Electrical Machines with the KU Leuven in Belgium. Since 2004, he is full professor and the director of the Institute of Electrical Machines (IEM) at RWTH Aachen University in Germany. 2006 he was vice dean of the faculty and from 2007 to 2009 he was the dean of the faculty of Electrical Engineering and Information Technology of RWTH Aachen University. His research interests are numerical field computation and optimization, the design and controls of electrical machines, in particular permanent magnet excited machines, induction machines and the design employing the methodology of virtual reality. Since several years Dr. Hameyer's work is concerned with the magnetic levitation for more than 250 journal publications, more than 500 international conference publications and author of 4 books. Dr. Hameyer is a member of VDE, IEEE senior member, fellow of the IET.